

Pore Structures and Fractal Dimensions in Early Permian Barakar Shales of Rajmahal Basin, Jharkhand, India

^{a,*}Subhashree Mishra, ^bApoorva Dixit, ^{c,d}Vivek Kumar Mishra, ^eVikram Partap Singh, ^cVinod Atmaram Mendhe

^aCSIR-National Institute of Oceanography, Dona Paula, Goa-403 004, India

^bDepartment of Geology, Banasthali Vidyapith, Niwai, Tonk, Rajasthan-304 022, India

^cCSIR-Central Institute of Mining and Fuel Research, Dhanbad, Jharkhand-826 015, India

^dAcademy of Scientific and Innovative Research, Ghaziabad-201 002, India

^eDST-Birbal Sahni Institute of Palaeosciences, 53-University Road, Lucknow-226 007, India

*Corresponding author E-mail: subhashree.geology@gmail.com , subhashree@nio.org

Abstract

The proximate, low pressure N₂ sorption, X-ray diffraction, and organic petrography parameters have been used to delineate the pore structures and fractal dimensions in the Barakar shales of Rajmahal Basin, India. The information has been utilized for the assessment of shale gas reservoir, and to know about the mode of occurrence and storage capacity of shales for the entrapment of methane (CH₄). The studied shales are characterized by high fixed carbon contents (10.14-46.09 wt.%), and contains significant abundance of brittle minerals, like quartz (6.0-51.6%) and mica (1.0-41.2%). The petrographic observations show that the studied samples comprise of numerous laths of vitrinite (collotelinite and vitrodetrinite) and semifusinite macerals, and quartz grains. The data of low-pressure N₂ sorption analysis indicates the shales encompass mainly meso- to macropores and microfractures. The total pore volume, average pore size and multipoint BET surface area of the studied shales vary from 0.012-0.023 cc/g, 8.295-10.840 nm, and 5.752-10.390 m²/g respectively. Two types of fractal dimensions (D₁ and D₂) have been calculated by using FHH (Frankel-Halsey-Hill) method from the N₂ adsorption isotherm. The high values of fractal dimensions (2.1949<D₁<2.4837 and 2.6668<D₂<2.7247) are indicating the highly rugged pore surface or complexity in the pore structures.

Keywords: Proximate analysis; X-Ray Diffraction; Adsorption-Desorption Isotherm; Macerals; Clay content; Shale gas; Lower Gondwana; Rajmahal Basin .

1. Introduction

The shale gas extraction is still in its beginning phase in India. Nevertheless, efforts have been made by several researchers for the evaluation of Indian shale deposits to delineate the prospective areas, housed formations, and estimate their hydrocarbon generation potentialities in regional and basinal scales (Sain et al., 2014; Hazra et al., 2015, 2018a, b; Mendhe et al., 2017a; Mishra et al., 2018a; Mishra et al., 2021; and many more). Subsequently, substantial developments have also been made on the characterization of thick shale associated sequences in many basins of India, such as Barakar and Barren Measures Formations in Damodar Basin (Varma et al., 2015; Mendhe et al., 2017a), Kommugudem and Raghavapuram Shales in Krishna-Godavari Basin (Padhy et al., 2013), Cambay Formation in Cambay Basin (Dayal et al., 2013; Hafiz et al., 2020), etc. In India, the total estimated recoverable reserve is approximately 96 trillion cubic feet from several identified Basins (mainly Cambay, Damodar and Krishna – Godavari) containing >300m thick organic rich shale (4-5% of organic content) (US EIA, 2015; Kumar et al., 2021). However, understanding the characteristic features of shale beds from the Rajmahal Basin is still far from satisfactory. The basin holds significant sequences of the Lower Gondwana (Permian) thick coal and shale horizons of Barakar Formation and patches of Karharbari Formation, overlain by the Upper Gondwana (Triassic) sediments. The shale associated with Early Permian Barakar Formation (Artinskian) is the main source-rock for hydrocarbons, and a major target for shale gas exploration in the basin.

Recently, Mathews et al. (2020) have discussed the origin of organic matters, depositional conditions, and palaeoclimatic variations of coal-bearing Barakar sediments in the Rajmahal Basin. Murthy et al. (2021) have presented evidences for the existence of wildfire activity in the sediments. In fact, the present study is the first attempt to delineate the pore and fractal attributes of the Barakar shales of the Rajmahal Basin. The main aims of this investigation are: (i) to characterize the pore size, pore structure, and surface area parameters to whether shales in the basin support gas storage and transport, (ii) to identify the heterogeneity, pore connectivity and fractal dimensions of the pores in shales, and (iii) to study the relationships between surface area, pore volume, pore size, and fractal characteristics with inorganic and organic contents.

2. Geological settings

The Rajmahal Basin lies within latitudes 24° 00′:25° 30′ N and longitudes 87° 00′:88° 00′ E, and confined under Rajmahal-Purnea graben extending over Jharkhand and West Bengal States of India (Fig. 1). The basin is oriented in N–S direction with easterly dipping step-fault systems and covered by soft sediments or laterite or alluvium (Ghose et al., 2017; Murthy et al., 2021). The total

area of the basin spreads over four districts of Jharkhand, i.e., Sahibganj, Pakur, Godda and Dumka, and comprises five coalfields namely Hura, Chuperbhita, Pachwara, Mahuagarhi and Brahmani (Raja Rao, 1987; Ghose et al., 1996). The basin is bounded by the river Ganges in the north, Rajmahal volcanics in the east, metamorphic in the west, and by laterite and alluvium in the south (Singh and Singh, 1996). The drainage pattern in the coalfield is controlled by the Ganga River flowing along the NE side of the basin (Coal Atlas of India, 1993). The Early Permian Barakar coal seams were delineated as a thin and irregular stretch on the western peripheries of the basin (Fig. 1). A generalized lithostratigraphic succession of the Rajmahal Basin has been enumerated in Table 1.

The basement was formed from the Archean rocks separated by a well-defined unconformity from the overlying Lower Gondwana sediments. The deposition of Gondwana sediments has been demarcated by the availability of patchy Talchir sediments along the western boundary of the basin, which is succeeded by the overlying Karharbari Formation (also a disseminated deposits), consisting of carbonaceous sandstones, grits and conglomerates. The thick coal and shale horizons of the Barakar Formation mainly spread conformably over the Archean basement (Raja Rao, 1987; Singh and Singh, 1996). The Permian sediments are overlain by the Late Triassic- Early Jurassic Dubrajpur and Rajmahal Formations, comprising of sandstones, siltstones, and clays/shales. The Early Cretaceous- Early Jurassic Rajmahal Traps and Intertrappean beds lie above the Upper Gondwana sediments, varying up to a thickness of 600 m.

3. Material and methods

For the study, a total of 13 core samples of shale housed in the Barakar Formation were systematically collected (between the depths 184.70 and 323.90 m) from an investigative exploratory borehole BH-1 drilled in the Bhalukasba Surni-I Block of Rajmahal Basin. The study area, lying near to the Chuperbhita Coalfield of Godda District, Jharkhand (Fig. 1), is a virgin location and as such no basic research on coal/shale has been carried out. The megascopic properties of shale cores, such as colour, banding pattern, grain size, lustre, fracture types, visible mineral association, plant-fossil imprint, etc. have been observed and recorded (Table 2).

3.1. Proximate analysis

The analysis has been carried out to determine the basic parameters like inherent moisture (IM) contents, ash yields, volatile matter (VM) yields and fixed carbon (FC) contents of the studied shales; following the Bureau of Indian Standard (IS: 1350-I, 1984). The representative shale samples were crushed, powdered and sieved with 72 mesh (~212 microns) size. For the determination of: i) IM content– the finely powdered sample (weighing about 1 g) was taken in the silica disc, and heated at a

temperature of $108^{\circ} \pm 2^{\circ} \text{C}$ in an oven for 1 hour; ii) ash yields– the sample was heated in a furnace (in presence of air) such that the temperature is increases to 500°C in 30 min. and then to $815^{\circ} \pm 15^{\circ} \text{C}$ in the next 30 min., and was further kept for 60 minutes; and iii) VM yields– the sample was placed in a furnace (in absence of air) at a temperature of $900^{\circ} \pm 10^{\circ} \text{C}$ for seven minutes. The fixed carbon content was estimated as $\text{FC} = 100 - (\text{M} + \text{Ash} + \text{VM}) \text{ wt.}\%$.

3.2. *Organic petrography*

The sample (850 μm to 1mm size) pellets preparation and maceral analysis have been performed by following the ISO 7404-2, 3 (2009) norms, respectively. The maceral description and terminology provided by the International Committee for Coal and Organic Petrology for the vitrinite (ICCP, 1998), liptinite (Pickel et al., 2017) and for the inertinite (ICCP, 2001) groups are followed. To signify the presence of organic matters, petrographic analysis has been conducted on a “Carl Zeiss Axio Imager M2m” microscope under both reflected white light and fluorescence blue light using an oil immersion lens (of 50x magnification). The macerals are identified following the above mentioned literatures to interpret the organic matter types, source and palaeodepositional conditions (Zhang et al., 2009; Suárez-Ruiz et al., 2012; Schieber, 2013).

3.3. *Low Pressure N₂ Sorption Isotherm analysis*

This analysis has been carried out for the determination of the quantity of gas adsorption and desorption, which further helps to measure the surface area, pore volume, pore size, pore structures and associated fractal characteristics (Kuila and Prasad, 2013; Mendhe et al., 2017a, b; Hazra et al., 2018a, 2019). According to the International Union of Pure and Applied Chemistry (IUPAC), the adsorption isotherms has been categorised into 6 types (as type I - type VI), while 4 types of desorption hysteresis loops (H1-H4; de Boer, 1958). The hysteresis patterns suggest about the pore structure and connectivity within the shale beds (Sing et al., 1985). The surface area available for gas adsorption within the organic and inorganic contents is influenced by the burial depths, kerogen types, maturities, clay minerals and moisture contents (Zhang et al., 2012; Cao et al., 2015).

The low pressure N₂ adsorption analysis has been performed by using Quantachrome AutosorbiQ™2MP-XR instrument. For the analysis, the studied shale cores were crushed and sieved (0.8-1.0 mm size). The prepared samples were kept in oven to dry at $105^{\circ} \pm 5^{\circ} \text{C}$ for 3 to 4 hrs. The samples were weighed and kept for degassing at about 300°C for 1 to 2 hrs. to remove impurities and the moisture content (Quantachrome, 2014; Mendhe et al., 2017a, 2018a, b). After degassing, the cell+sample were again weighed and placed tightly in analysis station for further sorption analysis. The analysis was done at a constant temperature using liquid nitrogen (-195.79°C or 77°K), and

relative pressure (P/P_0) range between 0.00 and 0.99. The surface area, was calculated from the sorption curve using Brunauer-Emmet-Teller (BET: 0.05-030) method (Brunauer et al., 1938); whereas, pore size distributions and pore volume were estimated under a relative pressure range of 0.35–0.99 using Barrett, Joyner and Halenda (BJH) method (Nelson, 2009; Barrett et al., 1951) and Density Functional Theory (DFT) method (Gregg and Sing, 1982).

The pore fractal dimension (D) has been calculated from the N_2 adsorption isotherm curves using FHH method (Yang et al., 2014; Mendhe et al., 2017b; Mishra et al., 2018a; Huang et al., 2020; Wang et al., 2021), and with the help of following expression:

$$\ln(V_{ads}) = A \left[\ln \left(\ln \left(\frac{P_0}{P} \right) \right) \right] + C$$

Where, V_{ads} = volume adsorbed at equilibrium pressure P , A = constant characteristic of a given adsorbent related to the fractal dimension D ($D= 3+A$), P_0 = saturated vapor pressure, C = constant.

According to the FHH model, D can be determined from the slope of the straight line in the plot of $\ln V_{ads}$ vs. $\ln(\ln(P_0/P))$.

3.4. X-ray Diffraction analysis

The method has been used to obtain information about the mineral/clay phases present in the studied shale samples. The X-ray Diffraction (XRD) analysis was carried out by using ‘Bruker D8 Advance’ (Germany Make) machine. Prior to analysis, the samples of grain size $<150 \mu\text{m}$ were dried at $60 \text{ }^\circ\text{C}$ temperature for one hour in hot air oven to release surface moisture. For performing the analysis, the 2-theta range was fixed from 10° to 70° with a scan step of $0.5^\circ/\text{s}$. The Rietveld refinement method has been used, and the obtained peaks are compared with a predefined theoretical profile for the semi-quantitative assessment of clay and mineral percentages (Rietveld, 1967; Mishra et al., 2018a).

4. Results

The studied shales of the Rajmahal Basin are characteristically light or dark grey to black in colour and carbonaceous in nature, containing a variable amount of minerals (clay, quartz, mica grain, etc.; Fig. 2). Thus, most of the core samples have shown dull lustre with brittle and flaky surficial features. The detail of megascopic parameters of the shale core samples are presented in Table 2.

4.1. Proximate constituent

The data of proximate analysis are summarised in Table 3. The inherent moisture contents, ash yields and volatile matter yields of the studied shale samples range from 5.32 to 9.42 wt.%, 18.88 to 72.28 wt.% and 12.27 to 25.62 wt.%, respectively. The samples have high fixed carbon contents, varying between 10.14 and 46.09 wt.%.

4.2. Maceral composition

The macerals observed/recorded in the studied samples are mainly in dispersed and detrital patterns. The shales chiefly contain macerals of the vitrinite group, followed by liptinite and inertinite groups. Among oxygen-rich vitrinites, the collotelinite and collodetrinite subgroups have shown dominant occurrences. The sporinite (spores-pollen) and alginite (algae) are the major macerals of hydrogen-rich liptinite group. The relatively carbon-rich inertinite group is represented by the macerals semifusinite, fusinite and inertodetrinite. The vitrinite particles are, generally, embedded in the groundmass of fusinite and semifusinite, besides clastic minerals. The inorganic/mineral matters identified are clay content, quartz, pyrite and mica. The representative photomicrographs of different macerals and mineral inclusions are illustrated in Fig. 3.

4.3. Surface area analysis

4.3.1. Pore volume, pore size and surface area

The pore volume, pore size, pore structures and the surface area are calculated by low pressure N₂ sorption (adsorption-desorption) method, and the results are enumerated in Table 4. The samples show type II adsorption isotherms signifying that the shales are dominated with meso- to macropore system, and desorption profiles display H3 hysteresis. This indicating the presence of plate-like divisions that leads to the development of slit-shaped pores (Sing et al., 1985; Mendhe et al., 2017c, 2018a, b; Fig. 4a–g).

The multipoint BET surface area of the samples varies from 5.752 to 10.390 m²/g (Table 4, Fig. 5). The mesopore surface area has also been determined following the single-point BET and the Langmuir methods, indicating divergent surface area values because of the heterogeneous composition of shale samples. The values of the single-point BET and Langmuir surface area of the shales range from 5.249 to 9.770 and 9.134 to 17.580 m²/g, respectively (Table 4). The adsorption of N₂ gas molecule largely within the relative pressure range of 0.05-0.35 is represented in the Langmuir plots (Fig. 6). The results of pore size as obtained from BJH (Barrett-Joyner-Halenda), DFT (density functional theory) and average pore diameter vary between 3.005 and 4.498, 1.410 and 4.125 and between 8.295 and 10.840 nm, respectively. The pore volume has been calculated by different methods

like BJH, DFT and total pore volume for the representative shale samples; varying from 0.010 to 0.020, 0.010 to 0.019 and 0.012 to 0.023 cc/g, respectively (Table 4). The micropore surface area and micropore volume has been calculated by using Harkins-Jura model following the de Boer et al. (1963) and the obtained results are presented in Table 4. The negative values for micropore surface area suggesting all the studied samples are devoid of micropores except the sample RB-5 shows presence of both micro-and mesopores (Scherdel et al., 2010; Mishra et al., 2018b).

4.3.2. Fractal dimension

The study of fractal characteristics or surface irregularities helps to understand the gas adsorption within pore-matrix system of shale beds for which FHH model has been considered to be the most accurate and widely accepted. The fractal dimension noted as 'D' value varies between 2 and 3 from a regular smooth to a highly rugged surfaces. The fractal dimension of the studied shale samples ranges from 2.1949 to 2.4837 (for D_1) and 2.6668 to 2.7247 (for D_2 , Table 5).

4.4. XRD analysis

The semiquantitative calculation of minerals and clay contents, as obtained from XRD peaks using Rietveld refinement method of the studied shale samples is given in Table 6. The contents of Quartz, Muscovite and Biotite range from 6.0 to 51.6%, 1.0 to 37.7% and 1.6 to 38.0%, respectively in the core samples. The carbonate mineral Siderite is found in only two samples RB-9 (5.9%) and RB-12 (11.9%). The contents of clay minerals like kaolinite, illite, vermiculite and montmorillonite vary between 15.7 and 49.5%, 3.2 and 35.6%, 0.6 and 30.5% and between 0.4 and 15.2%, respectively. The chlorite clay content is noticed in sample nos. RB-9 (23.7%) and RB-11 (21.1%).

5. Discussion

Shale gas is considered as one of the most vital non-conventional energy resources in the world. It is generated by the thermal degradation of vegetal/organic matters present in shale sequences, and trapped inside the micropore grid and fracture system of shale beds (Zhang et al., 2012; Yang et al., 2016; Mendhe et al, 2018b). Shales are having two basic units together controlling the structural characteristics and heterogeneity of the pores, that are organic matters (macerals= visual kerogen) and minerals (Curtis, 2002). In the studied Early Permian Barakar shales of Rajmahal Basin, vitrinite is the chief group of macerals present which is originated from the gymnosperm wood forests. The presence of vitrinite and the high contents of fixed carbon are suggesting the suitability of these shales for gas generation. This observation is in accordance with the earlier reports of Permian shales from the adjacent Raniganj and Jharia coal fields of Damodar Basin (Hazra et al., 2018c; Mendhe et al., 2017c).

Furthermore, several researchers have emphasized on the pore structures and fractal characterizations of shale beds for the gas adsorption/storage/transport (Curtis et al., 2012; Mishra et al., 2018a; Hazra et al., 2020; Wang et al., 2021). In the studied shales, the existence of slit-shaped pores indicates ease flow of gas through interconnected pore network (Kuila and Prasad, 2013). Groen et al. (2003) has suggested that the sorption hysteresis loop has been compressed as a result of fluctuating hemispheric circumference in the course of capillary condensation and evaporation in pores <4 nm and pressure range below 0.40, may be due to the application of tensile strength (Mendhe et al., 2018b; Boruah et al., 2019). The plots of multilayer (BET method) and monolayer (Langmuir method) show the availability of surface area for the storage of gas in the studied shales, yielding up to <10.5 m²/g and 18 m²/g, respectively. The differences in surface area values could be due to the monolayer adsorption covers over a wide area, whereas multilayer adsorption on the surface gas molecules physically stacked on one another.

The BJH pore size distribution shows that shales are having major distribution of pores within the size range of 2 to 10 nm, that is of mesoporous abundance (Fig. 7a–g). The graph signifies heterogeneity in pore size distribution caused by the variable clay and mineral assemblages, volatile matters and diagenetic effects (Boruah et al., 2019). The DFT method is robust for explaining the adsorption of N₂ molecule in shales containing both organic and inorganic matters (Mendhe et al., 2018b). In the studied shales, DFT plots showing that the micropores with pore width varying between 0 and 2 nm, and width 4 to 8 nm are more accountable for the adsorption of gas molecules (Fig. 8a–g). Recently, Wang et al. (2021) have also observed two noticeable peaks at approx. 1.5 nm and 4 to 7 nm pore sizes, along with comparatively smaller peaks at higher pore sizes while studied the shales from Sichuan Basin, China. Moreover, the decrease in pore volume along with the increase in pore diameter suggests the drop in the availability of micro- and mesopores (Brunauer et al., 1938; Curtis, 2002; Chen et al., 2016).

The sufficient pore volume and larger surface area is effective for the substantial gas adsorption and gas storage, whereas the availability of a good pore networking and fractals are beneficial for gas transportation (Zhang et al., 2016; Huang et al., 2020). Likewise, the FHH plots of the studied samples indicating that shales have two separate fractal dimensions at different pressure range (low pressure and high-pressure divisions), and the pore surface (D₁) is rough/rugged (Fig. 9). The available pore structures (D₂) in shales are heterogeneous and complex (Jiang et al., 2016; Hazra et al., 2018c; Chen et al., 2019). The plot of D₁ shows similar trend to that of D₂ in shales, indicating that the ruggedness of the pore surface is interrelated to the complexity of pore structure (Fig. 10). The fractal dimension D₁ vs. D₂ shows a strong positive correlation (Fig. 11) implying fractals in low- and high-pressure

range that leads to the ruggedness of pore surfaces and complex pore structures together (Chen et al., 2019). Similarly, two types of fractal dimensions have also been observed in the Longtan Shales (Middle Permian) of Guizhou, Southwest China (Huang et al., 2020), and Early Permian coal beds of West Bokaro, Jharkhand, India (Mendhe et al., 2017b).

Additionally, the dominance of different types of clay and associated minerals along with organic contents helps to characterize the source-rock, gas-flow and gas storage within the pores (Brooks, 1952; Slatt and Rodriguez 2012; Guo et al., 2014). The shale beds having quartz contents more than that of the clay contents are making the beds of brittle nature, which leads to easy fracturing through the target shale horizons. The peaks of XRD analysis of the studied Barakar shales (Fig. 12) are reflecting the abundance of kaolinite clay, and implies significant chemical weathering and diagenetic variation of the alumino-silicate minerals like potassium-feldspar and muscovite (Mendhe et al., 2017c; Mishra et al., 2018a; Mishra et al., 2021).

The depth vs. multipoint BET surface area and total pore volume showing a moderate positive correlation, and signifying carbonaceous shales (Fig. 13a–b), whereas the negative relationship with average pore size that illustrating with increasing depth (Fig. 13c) develops better pore connectivity availing storage space for the methane gas entrapment irrespective of the pore size distributions (Fig. 13a-c). The multipoint BET surface area showed a positive trend with average pore size, and a strong positive relationship with total pore volume $R^2= 0.83$, Fig. 13d); indicating that the shale beds with smaller average pore size have more abundant macropores and mesopores (Chen et al., 2016; Li et al., 2019). The scatter plot between multipoint BET surface area and fixed carbon content shows an average negative correlation ($R^2= 0.55$, Fig 13e), signifying that the organic matter does not support gas storage (Hazra et al., 2018b). Whereas, the BET plot shows a weak positive trend with the ash content that comparatively favouring adsorption of gas (Fig. 13f). A negative trend has also been observed among the estimated surface areas and organic contents for the shales/coals from India and Turkey, whereas positive correlation with the inorganic content is suggesting more influence of minerals and clays for hoisting pores than the organic matters (Hazra et al., 2020; and references therein).

Moreover, increasing trend of BET surface area with respect to the organic matters has already been stated by many workers (Yang et al., 2014; Shao et al., 2017; Tang et al., 2019; etc.), and no significant correlation has been observed by Sun et al. (2016) and Ross and Bustin (2009). The cross-plot between multipoint BET surface area and Langmuir surface area with quartz and total clay content shows a positive trend (Fig. 14a–b); elucidating increase in inorganic content raise the heterogeneity of shales, and leading to a higher possession of multilayer and monolayer surface areas (Zhang et al.,

2016). The average pore size has a negative trend with the quartz, while it shows positive relation with the clay minerals, and that leads to the development of significant micropores along with the influence of organic matters to the distribution of pores in the shales (Fig. 14c). However, total pore volume and clay or quartz are more or less independent to each other, and show no strong relationship (Fig. 14d). This elucidating that a single mineral doesn't play a noteworthy role while determining the total pore volume, but may only regulate certain types of pore development in the shales.

The fractal dimension especially signifies the irregularity (roughness) of the pore surface. The relationships between the BET surface area and depth with fractal dimensions (D_1 and D_2) of the studied shales are presented in Fig. 15a–b. Although, an average correlation exists between the fractal dimension (D_2) with depth and surface area, signifying that larger fractal dimensional have a greater surface area with an increase in depth. However, a strong negative correlation between average pore size and both the fractal dimensions (D_1 , D_2 ; Fig. 15c) is representing increasing fractal dimension associated with complicated pore structures, and development of the more meso- to macropores. Additionally, a moderate negative correlation of total pore volume with fractal dimensions signifying that decrease in the pore volume may be due to the abundance of mesopores, and complexity in pore structures that leads to the pore blocking (Mendhe et al., 2018b; Fig. 15d).

The overall correlations/observations of different parameters suggest that the combination of pore structures and fracture dimensions with different shapes and sizes revealing about the complicated pore–fracture system in the studied Barakar shales for the gas adsorption and transportation. Shales with a higher value of D_1 and D_2 (close to 3) leads to the development of more complexity of pore surface, pore structure and better pore networking; favouring free gas storage capacity (Wang et al., 2019). Therefore, the fractal dimensions and pore structures are important factors for the characterization of pores, and considered as major constraints to demonstrate the shale storage capacity. Hence, the study of pore structures and fractal dimensions would play a primary/vital role in detail characterization of the shale gas reservoirs. However, the study recommends that the SEM, low pressure CO_2 adsorption and high-pressure CH_4 adsorption characteristics should be well-performed on the shales of Rajmahal Basin in future for the economic considerations.

6. Conclusions

The shale core samples of Barakar Formation (Early Permian) from Rajmahal Basin have been evaluated to set on the effect of pore structures and fractal dimensions on shale gas storage capacity. Besides, to describe the organo-mineralogical assemblages of shales, pore characteristics and

parameters like inherent moisture, fixed carbon contents, etc. have also been considered. The investigation has obtained the following inferences:

- The presence of vitrinite group of macerals in shales is indicating dominant gas generation capacity.
- The shales contain mostly silt-shaped mesopores whereas the sample RB-5 comprises of both micro- and mesopores, and having BET multipoint surface area from 5.752 to 10.390 m²/g; signifying sufficient space for the gas storage.
- The fractal dimensions data are suggesting that the pore surfaces (D₁) are rough/rugged, and available pore structures (D₂) in shales are heterogeneous and complex.
- The abundance of kaolinite and chlorite clays is critical in storage and transport of gas within the shale horizons, and the availability of significant quartz contents makes the shale beds brittle, which may be helpful for the hydraulic fracturing during gas production.

Acknowledgements

We are thankful to Prof. S.K. Singh, Director, NIO (Goa) for his constant encouragements and support. We are also grateful to Dr. P.K. Singh, Director, CSIR-CIMFR (Dhanbad) for granting permission to carry out this work and adsorption-desorption analysis. The XRD analytical help by the Dept. of Physics, Banasthali Vidyapith (Rajasthan) is thankfully acknowledged. VPS thank Science and Engineering Research Board (SERB, Govt. of India) for providing the National Postdoctoral Fellowship (PDF/2018/000883).

Ethical Statements:

Conflict of Interest

The authors state that they have no known competing financial interests or personal relationships that could have appeared to influence the work reported in this article.

Funding

The authors have not received any financial support for research, authorship, and/or publication of this study.

References

1. Barrett, E.R., Joyner, L.G., Halenda, P.P., 1951. The determination of pore volume distribution in porous surfaces. *Journal of American Ceramic Society*, 73: 373-380.
2. Boruah, A., Rasheed, M.A., Mendhe, V.A., Ganapathi, S., 2019. Specific surface area and pore size distribution in gas shales of Raniganj Basin, India. *Journal of Petroleum Exploration and Production Technology*, 9: 1041-1050.
3. Brooks, B.T., 1952. Evidence of catalytic action in petroleum formation. *Industrial and Engineering Chemistry Research*, 44(11): 2570-2577.
4. Brunauer, S., Emmett, P.H., Teller, E., 1938. Adsorption of gases in multimolecular layers. *Journal of American Chemical Society*, 60(2): 309-319.
5. Cao, T.T., Song, Z.G., Wang, S.B., 2015. A comparative study of the specific surface area and pore structure of different shales and their kerogens. *Science China Earth Sciences*, 58(4): 510-522.
6. Chen, L., Jiang, Z., Jiang, S., Liu, K., Yang, W., Tan, J., Gao, F., 2019. Nanopore structure and fractal characteristics of lacustrine shale: Implications for shale gas storage and production potential. *Nanomaterials*, 9(3): 1-20.
7. Chen, Q., Zhang, J., Tang, X., Li, W., Li, Z., 2016. Relationship between pore type and pore size of marine shale: An example from the Sinian–Cambrian Formation, upper Yangtze region, South China. *International Journal of Coal Geology*, 158: 13-28.
8. Coal Atlas of India, 1993. Coal Atlas of India. Central Mine Planning and Design Institute, Ranchi Publication, pp. 1-139.
9. Curtis, J.B., 2002. Fractured shale-gas systems. *American Association of Petroleum Geologists Bulletin*, 86: 1921-1938.
10. Curtis, M.E., Cardott, B.J., Sondergeld, C.H., Rai, C.S., 2012. Development of organic porosity in the Woodford Shale with increasing thermal maturity. *International Journal of Coal Geology*, 103: 26-31.
11. Dayal, A.M., Mani, D., Mishra, S., Patil, D.J., 2013. Shale gas prospects of the Cambay Basin, western India. *Geohorizon*, 18(1): 26-31.
12. de Boer, J.H., 1958. The structure and properties of porous materials. In: Everett, D.H., Stone, F.S., (Eds.), Butterworths, London, p. 68.
13. de Boer, J.H., Lippens, B.C., Linsen, B.G., Broekhoff, J.C.P., van den Heuvel, A., Osinga, Th, J., 1963. The t-curve of multimolecular N₂-adsorption. *Journal of colloid and interface science*. 21, 405-414.
14. Ghose, N.C., Chatterjee, N., Windley, B.F., 2017. Subaqueous early eruptive phase of the late Aptian Rajmahal volcanism, India: Evidence from volcanoclastic rocks, bentonite, black shales, and oolite. *Geoscience Frontiers*, 8(4): 809-822.
15. Ghose, N.C., Singh, S.P., Singh, R.N., Mukherjee, D., 1996. Flow stratigraphy of selected sections of the Rajmahal basalts, eastern India. *Journal of Southeast Asian Earth Sciences*, 13: 83-93.
16. Gregg, S.J., Sing, K.S.W., 1982. Adsorption, Surface Area and Porosity. In: 2nd Edn, Academic Press, London, pp. 98.
17. Groen, J., Peffer, L.L.A., Pérez-Ramírez, J., 2003. Pore size determination in modified micro- and mesoporous materials: Pitfalls and limitations in gas adsorption data analysis. *Microporous and Mesoporous Materials*. 60(1-3): 1-17.
18. Guo, X., Li, Y., Liu, R., 2014. Characteristics and controlling factors of micropore structures of the Longmaxi shale in the Jiaoshiba area, Sichuan Basin. *Natural Gas Industry*, 1(2): 165-171.
19. Hafiz, M., Hakhoo, N., Bhat, G.M., Kanungo, S., Thusu, B., Craig, J., Ahmed, W., 2020. Source potential and reservoir characterization of the Cambay Shale, Cambay Basin, India: Implications for tight gas and tight oil resource development. *American Association of Petroleum Geologists Bulletin*, 104: 1707-1749.

20. Hazra, B., Chandra, D., Singh, A.K., Varma, A.K., Tiwari, D., Singh, P.K., Buragohain, J., Boral, P., 2019. Comparative pore structural attributes and fractal dimensions of Lower Permian organic-matter-bearing sediments of two Indian basins: Inferences from nitrogen gas adsorption. *Energy Sources, Part A: Recovery, Utilization and Environmental Effects*, ISSN: 1556-7036.
21. Hazra, B., Varma, A.K., Bandopadhyay, A.K., Mendhe, V.A., Singh, B.D., Saxena, V.K., Samad, S.K., Mishra, D.K., 2015. Petrographic insights of organic matter conversion of Raniganj Basin shales, India. *International Journal of Coal Geology*, 150-151: 193-209.
22. Hazra, B., Vishal, V., Singh, D.P., 2020. Applicability of low-pressure CO₂ and N₂ adsorption in determining pore attributes of organic-rich shales and coals. *Energy & Fuels*, 35(1): 456-464.
23. Hazra, B., Wood, D.A., Kumar, S., Saha, S., Dutta, S., Kumari, P., Singh, A.K., 2018a. Fractal Disposition and Porosity Characterization of Lower Permian Raniganj Basin Shales, India. *Journal of Natural Gas Science and Engineering*, 59: 453-465.
24. Hazra, B., Wood, D.A., Vishal, V., Singh, A.K., 2018c. Pore Characteristics of Distinct Thermally Mature Shales: Influence of Particle Size on Low-Pressure CO₂ and N₂ Adsorption. *Energy & Fuels*, 32(8).
25. Hazra, B., Wood, D.A., Vishal, V., Varma, A.K., Sakha, D., Singh, A.K., 2018b. Porosity controls and fractal disposition of organic-rich Permian shales using low-pressure adsorption techniques. *Fuel*, 220: 837-848.
26. Huang, Y., Zhang, P., Zhang, J., Tang, X., Liu, C., Yang, J., 2020. Fractal characteristics of pores in the Longtan shales of Guizhou, southwest China. *Geofluids*, Article ID 8834758: 1-16.
27. ICCP (International Committee for Coal and Organic Petrology), 1998. The new vitrinite classification (ICCP System 1994). *Fuel*, 7: 349-358.
28. ICCP (International Committee for Coal and Organic Petrology), 2001. The new inertinite classification (ICCP System 1994). *Fuel*, 80: 459-471.
29. ISO 1350-1, 1984. Methods of test for coal and coke, Part I: Proximate analysis. Solid Mineral Fuels Sectional Committee, PCDC 7, 1-34.
30. ISO 7404-2, 2009. Methods for the petrographic analysis of coals— Part 2: Methods of preparing coal samples.
31. ISO 7404-3, 2009. Methods for the petrographic analysis of coals — Part 3: Method of determining maceral group composition.
32. Jiang, F.J., Chen, D., Chen, J., Li, Q.W., Liu, Y., Shao, X.H., Hu, T., Dai, J.X., 2016. Fractal analysis of shale pore structure of continental gas shale reservoir in the Ordos Basin, NW China. *Energy & Fuels*, 30: 4676-4689.
33. Kuila, U., Prasad, M., 2013. Specific surface area and pore-size distribution in clays and shales. *Geophysical Prospecting*, 61: 341-362.
34. Kumar, S., 2021. Insights of Shale Gas Exploration and Development in India: Review. *International Journal of Scientific Research*, 10(5): 14-16.
35. Li, Z., Jiang, Z., Yu, H., Liang, Z., 2019. Organic matter pore characterization of the Wufeng-Longmaxi shales from the Fuling Gas Field, Sichuan Basin: Evidence from organic matter isolation and low-pressure CO₂ and N₂ adsorption. *Energies*, 12(7): 1207.
36. Mathews, R.P., Pillai, S.S.K., Manoj, M.C., Agrawal, S., 2020. Palaeoenvironmental reconstruction and evidence of marine influence in Permian coal-bearing sequence from Lalmatia Coal mine (Rajmahal Basin), Jharkhand, India: A multi-proxy approach. *International Journal of Coal Geology*, 224: 1-14.
37. Mendhe, V.A., Bannerjee, M., Varma, A.K., Kamble, A.D., Mishra, S., Singh, B.D., 2017b. Fractal and pore dispositions of coal seams with significance to coalbed methane plays of East Bokaro, Jharkhand, India. *Journal of Natural Gas Science Engineering*, 38: 412-433.
38. Mendhe, V.A., Kumar, V., Saxena, V.K., Banerjee, M., Kamble, A.D., Singh, B.D., Mishra, S., Sharma, S., Kumar, J., Varma, A.K., Mishra, D.K., Samad, S.K., 2018a. Evaluation of gas

- resource potentiality, geochemical and mineralogical characteristics of Permian shale beds of Latehar-Auranga Coalfield, India. *International Journal of Coal Geology*, 196: 43-62.
39. Mendhe, V.A., Mishra, S., Khangar, R.G., Kamble, A.D., Kumar, D., Varma, A.K., Singh, H., Kumar, S., Banerjee, M., 2017c. Organo-petrographic and pore facets of Permian shale beds of Jharia Basin with implications to shale gas reservoir. *Journal of Earth Science*, 28: 897-916.
 40. Mendhe, V.A., Mishra, S., Varma, A.K., Kamble, A.D., Bannerjee, M., Singh, B.D., Sutay, T., Singh, V.P., 2018b. Geochemical and petrophysical characteristics of Permian shale gas reservoirs of Raniganj Basin, West Bengal, India. *International Journal of Coal Geology*, 188: 1-24.
 41. Mendhe, V.A., Mishra, S., Varma, A.K., Kamble, A.D., Bannerjee, M., Sutay, T., 2017a. Gas reservoir characteristics of the Lower Gondwana shales in Raniganj Basin of Eastern India. *Journal of Petroleum Science Engineering*, 149: 649-664.
 42. Mishra, D.K., Samad, S. K., Varma, A. K., Mendhe, V. A., 2018b. Pore geometrical complexity and fractal facets of Permian shales and coals from Auranga Basin, Jharkhand, India. *Journal of Natural Gas Science and Engineering*, 52: 25-43.
 43. Mishra, D.K., Varma, A.K., Mendhe, V.A., Agrawal, S., Singh, B.D., Hackley, P.C., 2021. Organo-facies and mineral effects on sorption capacity of low-maturity Permian Barakar shales from the Auranga Basin, Jharkhand, India. *Energy & Fuels*, 35(9): 7717-7737.
 44. Mishra, S., Mendhe, V.A., Varma, A.K., Kamble, A.D., Sharma, S., Bannerjee, M., Kalpana, M.S., 2018a. Influence of organic and inorganic content on fractal dimensions of Barakar and Barren Measures shale gas reservoirs of Raniganj Basin, India. *Journal of Natural Gas Science Engineering*, 49: 393-409.
 45. Murthy, S., Mendhe, V.A., Uhl, D., Mathews, R.P., Mishra, V.K., Gautam, S., 2021. Palaeobotanical and biomarker evidence for Early Permian (Artinskian) wildfire in the Rajmahal Basin, India. *Journal of Palaeogeography*, 10(5): 1-21.
 46. Nelson, P.H., 2009. Pore throat sizes in sandstones, tight siltstones, and shale. *American Association of Petroleum Geologists Bulletin*, 93(3): 329-340.
 47. Padhy, P.K., Das., S.K., Kumar, A., 2013. Krishna-Godavari continental rift basin: Shale gas and oil play system. 10th Biennial International Conference & Exposition on Petroleum Geophysics, SPG, Kochi, 1-6.
 48. Pickel, W., Kus, J., Flores, D., Kalaitzidis, S., Christanis, K., Cardott, B.J., Misz-Kennan, M., Rodrigues, S., Hentschel, A., Hamor-Vido, M., Crosdale, P., Wagner, N., 2017. Classification of liptinite– ICCP System 1994. *International Journal of Coal Geology*, 169: 40-61.
 49. Quantachrome, 2014. Characterising porous materials and powders-AutosorbiQ and ASiQwin gas sorption system operating manual, 2: 199-426.
 50. Raja Rao, C.S., 1987. *Bulletins of the Geological Survey of India. Series A, No.45. Coalfields of India. Vol. IV. Pt. I. Coal Resources of India (excluding Dhanbad district)*, 336p.
 51. Rietveld, H.M., 1967. Line profiles of neutron powder-diffraction peaks for structure refinement. *Acta Crystallographica*, 22(1): 151-152.
 52. Ross, D.J.K., Bustin, R.M., 2009. The importance of shale composition and pore structure upon gas storage potential of shale gas reservoirs. *Marine and Petroleum Geology*, 26: 916-927.
 53. Sain, K., Rai, M., Sen, M.K., 2014. A review on shale gas prospect in Indian sedimentary basins. *Journal of Indian Geophysical Union*, 18(2): 183-194.
 54. Scherdel, C., Reichenauer, G., Wiener, M., 2010. Relationship between pore volumes and surface areas derived from the evaluation of N₂-sorption data by DR-, BET and t-plot. *Microporous and Mesoporous Materials*, 132: 572–575.
 55. Schieber, J., 2013. SEM observations on ion-milled samples of Devonian Black Shales from Indiana and New York: The petrographic context of multiple pore types. In: Camp, W., Diaz, E., Wawak, B. (Eds.), *Electron Microscopy of Shale Hydrocarbon Reservoirs*. American Association of Petroleum Geologists Memoir, 102: 153-171.

56. Shao, X., Pang, X., Li, Q., Wang, P., Chen, D., Shen, W., 2017. Pore structure and fractal characteristics of organic-rich shales: A case study of the lower Silurian Longmaxi shales in the Sichuan Basin, SW China. *Marine and Petroleum Geology*, 80: 192-202.
57. Sing, K.S.W., Everett, D.H., Haul, R.A.W., Moscou, L., Pierotti, R.A., Rouquerol, J., Siemieniewska, T., 1985. Reporting physisorption data for gas–solid systems. *Pure and Applied Chemistry*, 57: 603-619.
58. Singh, M.P., Singh, P. K., 1996. Petrographic characterization and evolution of the Permian coal deposits of the Rajmahal Basin, Bihar, India. *International Journal of Coal Geology*, 29(1-3): 93-118.
59. Slatt, M., Rodriguez, N.D., 2012. Comparative sequence stratigraphy and organic geochemistry of gas shales: Commonality or coincidence? *Journal of Natural Gas Science and Engineering*, 8: 68-64.
60. Suárez-Ruiz, I., Flores, D., Mendonça Filho, J.G., Hackley, P.C., 2012. Review and update of the applications of organic petrology: Part 1, geological applications. *International Journal of Coal Geology*, 99: 54-112.
61. Sun, M., Yu, B., Hu, Q., Chen, S., Xia, W., Ye, R., 2016. Nanoscale pore characteristics of the Lower Cambrian Niutitang Formation Shale: A case study from Well Yuke #1 in the Southeast of Chongqing, China. *International Journal of Coal Geology*, 154-155: 16-29.
62. Tang, X., Jiang, Z., Jiang, S., Cheng, L., Zhong, N., Tang, L., Chang, J., Zhou, W., 2019. Characteristics, capability, and origin of shale gas desorption of the Longmaxi Formation in the southeastern Sichuan Basin, China. *Scientific Report*, 9: 1-16.
63. US EIA (Energy Information Administration) 2015. Annual Energy Outlook 2015 (AEO2015) With Projections to 2040. 154p.
64. Varma, A.K., Biswal, S., Hazra, B., Mendhe, V.A., Misra, S., Samad, S.K., Singh, B.D., Dayal, A.M., Mani, D., 2015. Petrographic characteristics and methane sorption dynamics of coal and shaly-coal samples from Ib Valley Basin, Odisha, India. *International Journal of Coal Geology*, 141-142: 51-62.
65. Wang, M., Xie, W., Huang, K., Dai, X., 2019. Fine characterization of lithofacies and pore network structure of continental shale: Case study of the Shuinan Formation in the north Jiaolai Basin, China. *Journal of Petroleum Science and Engineering*, 175: 948-960.
66. Wang, Y., Liu, L., Cheng, H., 2021. Gas adsorption characterization of pore structure of organic-rich shale: Insights into contribution of organic matter to shale pore network. *Natural Resources Research*, 30: 2377-2395.
67. Yang, F., Ning, Z., Liu, H. 2014. Fractal characteristics of shales from a shale gas reservoir in the Sichuan Basin, China. *Fuel*, 115: 378-384.
68. Yang, F., Ning, Z., Wang, Q., Liu, H., 2016. Pore structure of Cambrian shales from the Sichuan Basin in China and implications to gas storage. *Marine and Petroleum Geology*, 70: 14-26.
69. Zhang, L., Liu, Q., Zhu, R., Li, Z., Lu, X., 2009. Source rocks in Mesozoic–Cenozoic continental rift basins, east China: A case from Dongying Depression, Bohai Bay Basin. *Organic Geochemistry*, 40: 229-242.
70. Zhang, T., Ellis, S.G., Ruppel, S.C., Milliken, K., Yang, R., 2012. Effect of organic-matter type and thermal maturity on methane adsorption in shale-gas systems. *Organic Geochemistry*, 47: 120-131.
71. Zhang, Y., Shao, D., Yan, J., Jia, X., Li, Y., Yu, P., Zhang, T., 2016. The pore size distribution and its relationship with shale gas capacity in organic-rich mudstone of Wufeng-Longmaxi Formations, Sichuan Basin, China. *Journal of Natural Gas Geoscience*, 1: 213-220.

Table 1: Generalised stratigraphic succession of Rajmahal Basin (after Singh and Singh, 1996).



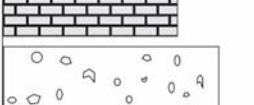
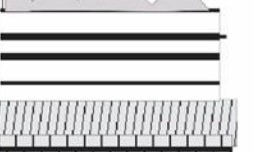



Rajmahal basin generalized borehole log	Formation	Lithological characters	Age	Thickness (m)
	Alluvium	Loose soil, silt and clay	Recent to Sub-recent	Upto 80 m
----- Unconformity -----				
	Rajmahal Traps and Intertrappeans	Flow of basalt, pitchstone and Intertrappean beds	Early Cretaceous to Early Jurassic	600 m
	Dubrajpur	Pebbly sandstone, coarse to medium grained sandstone, red siltstone	Late Triassic	60 to 250 m
----- Unconformity -----				
	Barakar	Coarse to medium grained sandstone, pebbly sandstone, grey shales clay and coal seams	Early Permian	250 to 550 m
	Karharbari	Grits, conlomerates and carbonaceous sandstone		
	Talchir	Tillite, fine to medium grained sandstone, olive green shale	Lower Carboniferous	
----- Unconformity -----				
		Basic rocks, amphibolites, band of quartzite, limestone, gneisses and granite	Archean	-

Table 2: Megascopic details of the studied shale core samples from Rajmahal Basin.

Area	Borehole No.	Sample Code No.	Formation	Depth (m)	Sample Type	Megascopic Properties
Bhalukasba Surni Block-1	MBSIR-141 (P-21) BH-1	RB-1	Barakar	184.70	Shaly Coal	Fine grain, greyish black in color, dull/earthy lusture, uneven to subconchoidal fracture, non-banded (thin parting of vitrain), two set of cleats
		RB-2		273.10	Carbonaceous Shale	Fine Grain, greyish black in color, dull/earthy lusture, uneven to subconchoidal fracture, non-banded, cleats
		RB-3		277.30	Shaly Coal	Very fine, black in color, sub-metallic lusture, uneven to subconchoidal fracture, non-banded
		RB-4		279.30	Shaly Coal	Fine grain, black in color, dull/earthy lusture, uneven to subconchoidal fracture, non-banded (Thin Parting), cleats
		RB-5		281.80	Shaly Coal	Fine grained, jet black in color, metallic lusture, uneven to subconchoidal fracture, non-banded, leaf impressions with tint of mica
		RB-6		290.30	Carbonaceous Shale	Fine Grain, black in color, dull/earthy lusture, uneven to subconchoidal fracture, non-banded, Cleats
		RB-7		294.20	Carbonaceous Shale	Fine grain, jet black in color, submetallic lusture, uneven to subconchoidal fracture, non-banded (parting of coal), cleats
		RB-8		298.70	Shale	Fine grained, black in color, dull /earthy lusture, uneven to subconchoidal fracture, non-banded, leaf impressions
		RB-9		302.60	Shaly Coal	Fine grained, jet black in color, dull /earthy lusture, uneven to even fracture, non-banded, cleats, leaf impression
		RB-10		307.10	Shaly Coal	Fine grained, jet black in color, dull/earthy lusture, uneven to even fracture, non-banded, leaf impressions
		RB-11		311.30	Shaly Coal	Fine grain, black in color, dull/earthy lusture, uneven to subconchoidal fracture, non-banded
		RB-12		319.80	Shaly Coal	Very fine, greyish black in color, dull /earthy lusture, uneven to subconchoidal fracture, non-banded, parting of coal present
		RB-13		323.90	Carbonaceous Shale	Fine grain, greyish black in color, dull/earthy lusture, uneven to subconchoidal fracture, non-banded, leaf impression

Table 3: Results of proximate analysis of studied shale core samples.

Sample No.	As Received Basis (wt. %)			
	IM	Ash	VM	FC
RB-1	5.32	72.28	12.27	10.14
RB-2	7.57	40.73	19.50	32.21
RB-3	7.92	29.88	22.38	39.83
RB-4	8.05	32.04	23.26	36.65
RB-5	9.21	21.66	24.66	44.47
RB-6	8.17	30.86	20.17	40.80
RB-7	9.42	18.88	25.62	46.09
RB-8	6.84	44.02	17.59	31.56
RB-9	6.07	48.69	17.56	27.69
RB-10	8.27	27.36	22.22	42.15
RB-11	7.06	41.01	19.06	32.87
RB-12	6.00	48.33	21.47	24.21
RB-13	7.24	35.68	24.43	32.66

Explanation: - IM: Inherent Moisture; VM: Volatile Matter; FC: Fixed Carbon.

Table 4: Results of low pressure N₂ adsorption isotherms of studied shale core samples.

Sample No.	Isotherms and Hysteresis Curve	Surface Area (m ² /g)				Pore Size (nm)			Pore Volume (cc/g)			
		Multi point BET	Single point BET	Langmuir	Micropore	BJH	DFT	Avg. pore	BJH	DFT	Total pore volume	Micropore volume
RB-2	II/H3	7.293	7.078	12.630	-0.247	4.498	1.410	8.503	0.014	0.013	0.0155	-0.0031
RB-4	II/H3	7.011	6.557	11.830	-0.278	3.763	1.410	8.510	0.013	0.012	0.0149	-0.0005
RB-5	II/H3	5.752	5.249	9.134	0.254	3.010	1.410	8.295	0.010	0.010	0.0119	-0.0002
RB-8	II/H3	5.890	5.555	9.979	-0.132	3.009	1.410	8.467	0.011	0.010	0.0125	-0.0003
RB-9	II/H3	7.254	6.678	13.390	-2.941	3.007	4.152	10.840	0.019	0.017	0.0197	-0.0020
RB-11	II/H3	8.172	7.848	13.370	-0.621	3.007	1.410	8.909	0.016	0.015	0.0182	-0.0007
RB-12	II/H3	10.390	9.770	17.850	-0.803	3.005	1.410	8.672	0.020	0.019	0.0225	-0.0009

Explanation: - BET: Brunauer-Emmett-Teller; BJH: Barrett-Joyner-Halenda; DFT: Density functional theory; Avg.: Average.

Table 5: Fractal fitting equations and fractal values for studied shale core samples.

Sample No.	Region I (D ₁)			Region II (D ₂)		
	Fractal fitting equation	Fitting Coefficient	D ₁ = 3+A ₁	Fractal fitting equation	Fitting coefficient	D ₂ = 3+A ₂
RB-2	$y = -0.5850x + 0.2065$	$R^2 = 0.9770$	2.4150	$y = -0.2816x + 0.3647$	$R^2 = 0.9524$	2.7184
RB-4	$y = -0.6252x + 0.1606$	$R^2 = 0.9737$	2.3748	$y = -0.2866x + 0.3298$	$R^2 = 0.9456$	2.7134
RB-5	$y = -0.5163x + 0.1019$	$R^2 = 0.9743$	2.4837	$y = -0.2753x + 0.2276$	$R^2 = 0.9489$	2.7247
RB-8	$y = -0.6167x + 0.0897$	$R^2 = 0.9767$	2.3833	$y = -0.2823x + 0.2603$	$R^2 = 0.9486$	2.7177
RB-9	$y = -0.8051x + 0.102$	$R^2 = 0.9624$	2.1949	$y = -0.3332x + 0.3556$	$R^2 = 0.9438$	2.6668
RB-11	$y = -0.5780x + 0.2465$	$R^2 = 0.9791$	2.4220	$y = -0.2971x + 0.3942$	$R^2 = 0.9554$	2.7029
RB-12	$y = -0.6013x + 0.3401$	$R^2 = 0.9807$	2.3987	$y = -0.3105x + 0.4881$	$R^2 = 0.9645$	2.6895

Table 6: Results of XRD analysis of shale core samples.

Sample No.	Quartz (%)	Kaolinite (%)	Illite (%)	Vermiculite (%)	Montmorillonite (%)	Chlorite (%)	Total clay (%)	Muscovite (%)	Biotite (%)	Total Mica (%)	Siderite (%)
RB_1	51.6	44.2	3.6	0.6	-	-	48.4	-	-	-	-
RB_2	34.3	31.1	3.4	7.3	8.4	-	50.2	13.9	1.6	15.5	-
RB_3	27.5	15.7	11.0	30.5	1.3	-	58.5	4.0	10.0	14.0	-
RB_4	34.4	28.2	9.3	1.1	-	-	38.6	27.0	-	27	-
RB_5	26.7	18.3	13.3	8.1	-	-	39.7	-	33.6	33.6	-
RB_6	45.3	40.2	-	10.4	1.3	-	51.9	-	2.8	2.8	-
RB_7	6.0	40.4	35.6	7.2	-	-	83.2	-	10.8	10.8	-
RB_8	8.7	21.3	25.8	3.0	-	-	50.1	22.9	18.3	41.2	-
RB_9	15.4	35.2	-	3.6	15.2	23.7	77.7	1.0	-	1	5.9
RB_10	29.0	27.3	3.2	0.8	0.4	-	31.7	1.3	38.0	39.3	-
RB_11	16.2	49.5	11.1	2.1	-	21.1	83.8	-	-	-	-
RB_12	38.8	29.1	10.1	3.6	4.6	-	47.4	1.9	-	1.9	11.9
RB_13	24.8	29.6	7.2	0.7	-	-	37.5	37.7	-	37.7	-

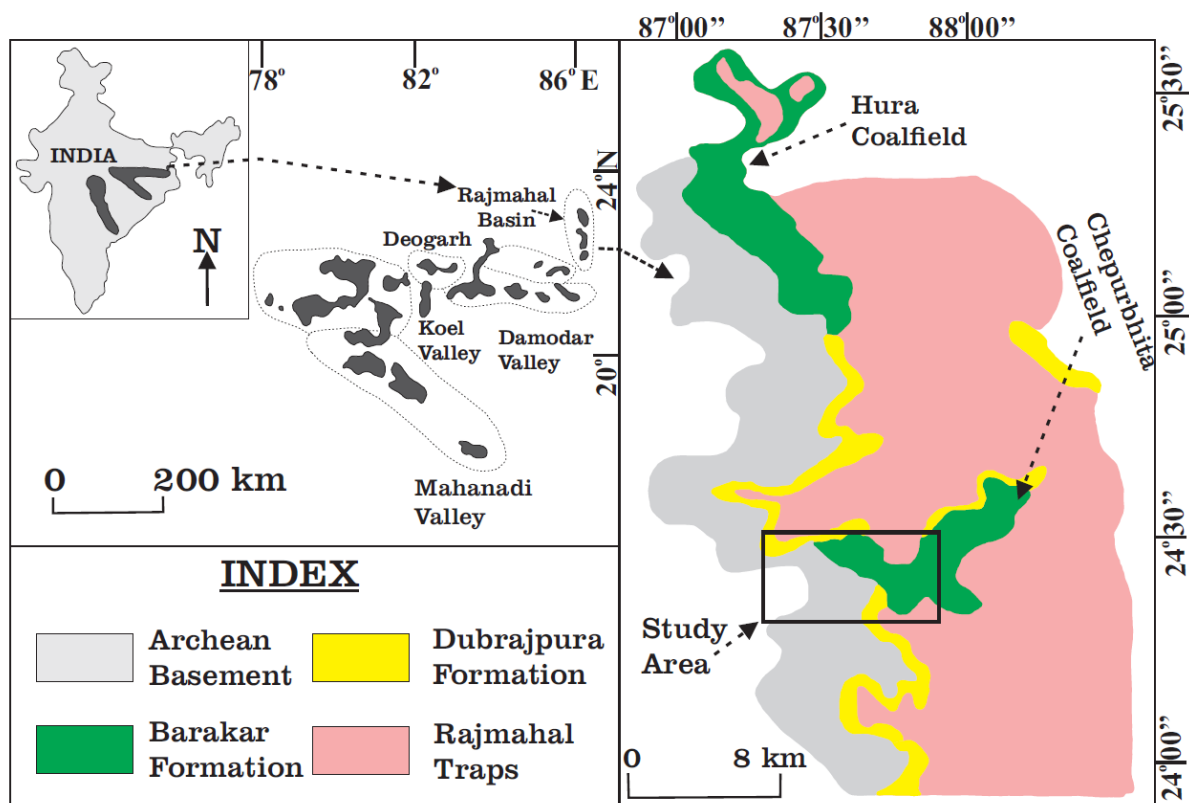


Fig. 1: Geological map of Rajmahal Basin showing study area (after Ghose et al., 1996; Singh and Singh, 1996).



Fig. 2: Megascopic photographs of the studied shale core samples collected from Rajmahal Basin.

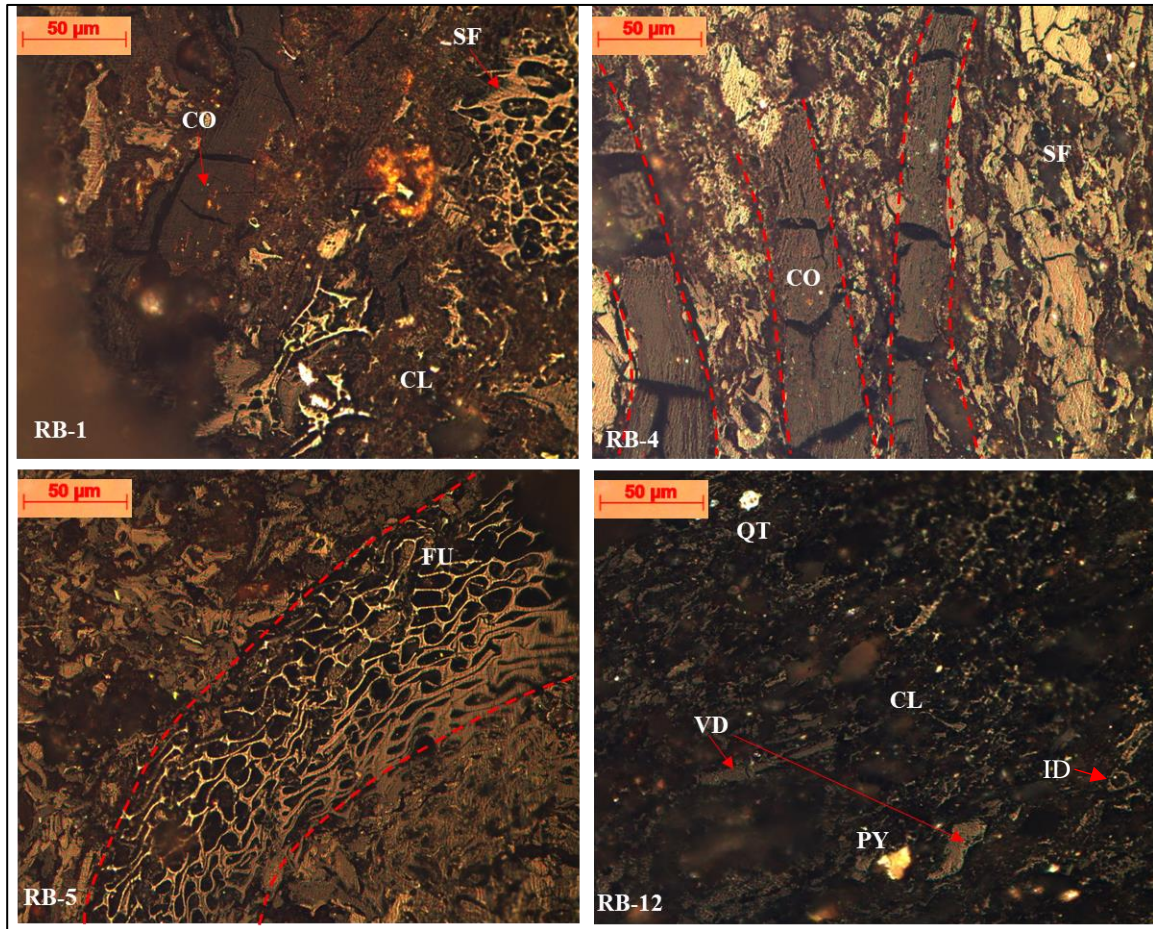


Fig. 3: Microscopic photographs Photomicrographs of macerals from Barakar shales of Rajmahal basin Basin.

Explanations: collotelinite (CO), vitrodetrinite (VD), semifusinite (SF), fusinite (FU) and clay (CL), quartz (QT), pyrite (PY), secretinite (SE) inertodetrinite (ID).

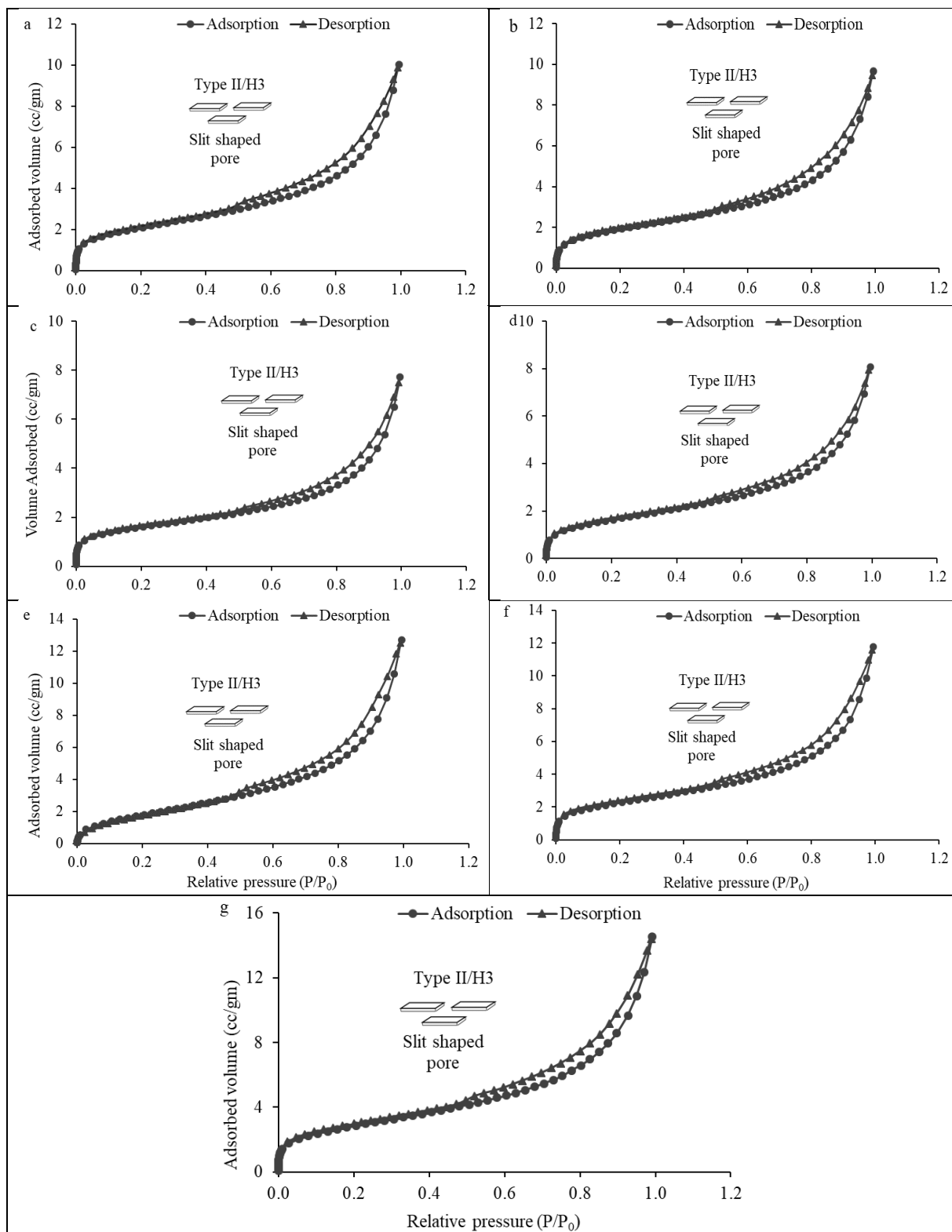


Fig. 4: Low pressure N_2 sorption isotherms for Barakar Formation shales indicating type II isotherm; H3 hysteresis pattern showing presence of slit shaped pores.

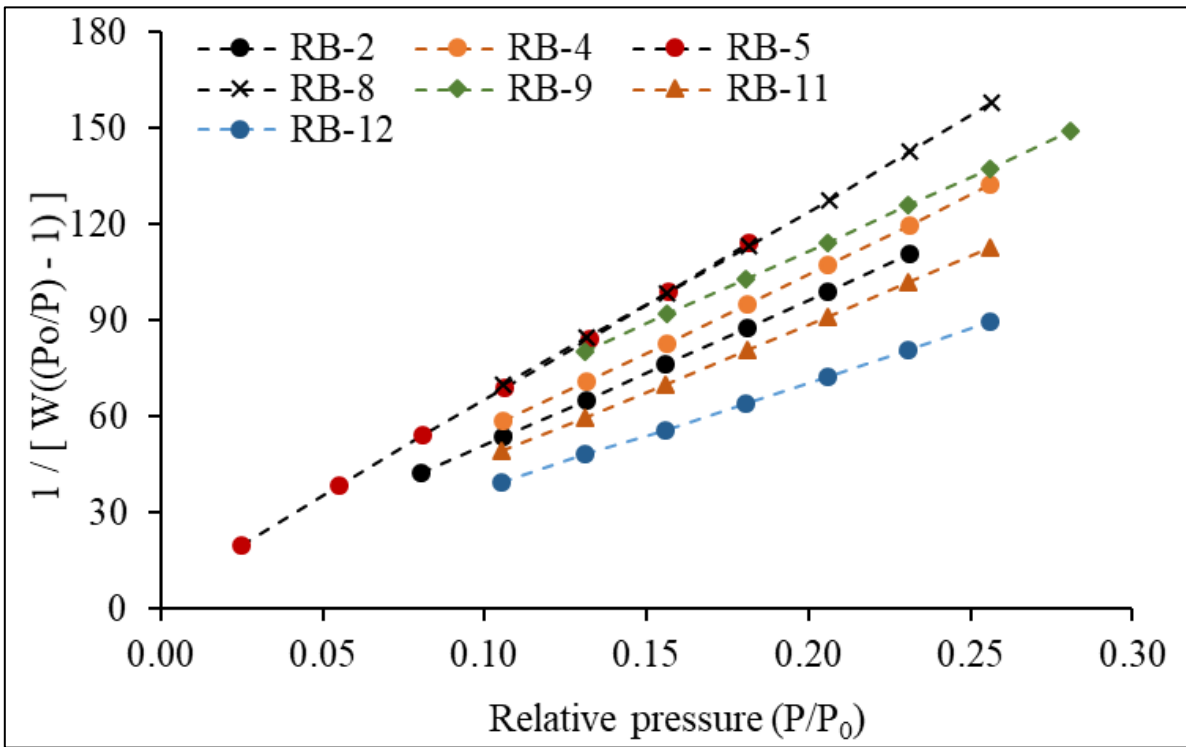


Fig. 5: Multipoint BET surface area plots for surface area determination of Barakar shales.

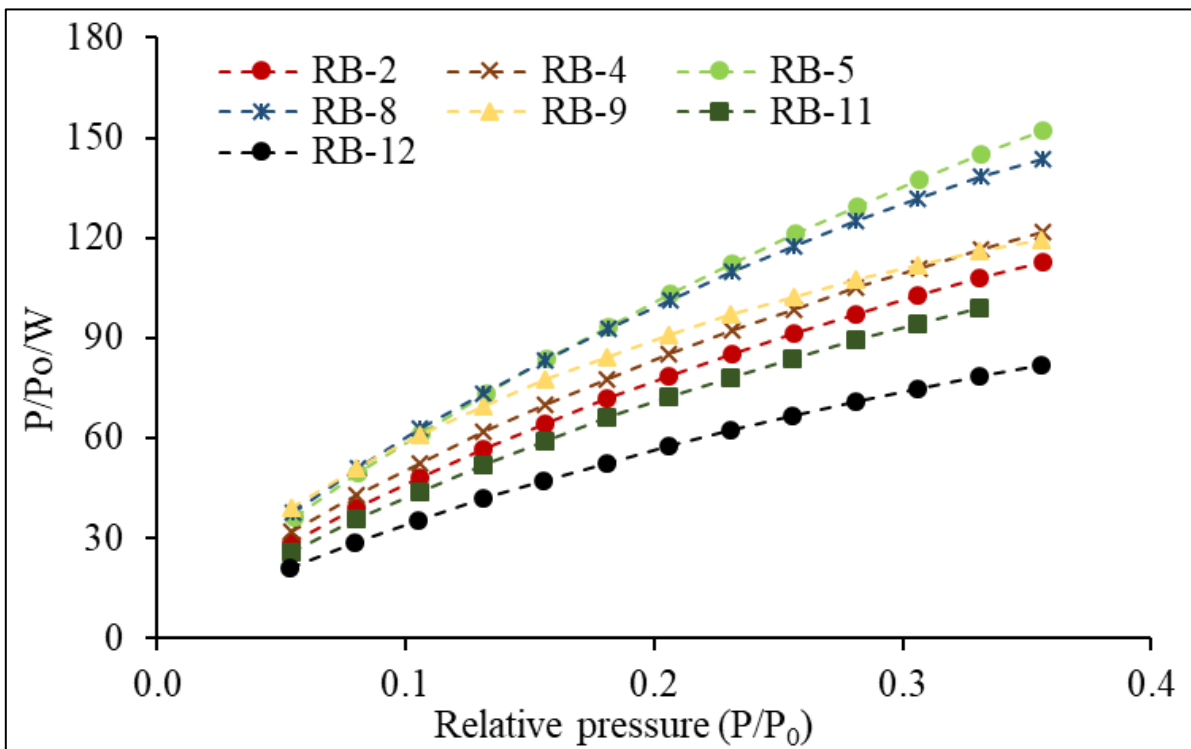


Fig. 6: Langmuir surface area plots for Barakar shales from Rajmahal Basin.

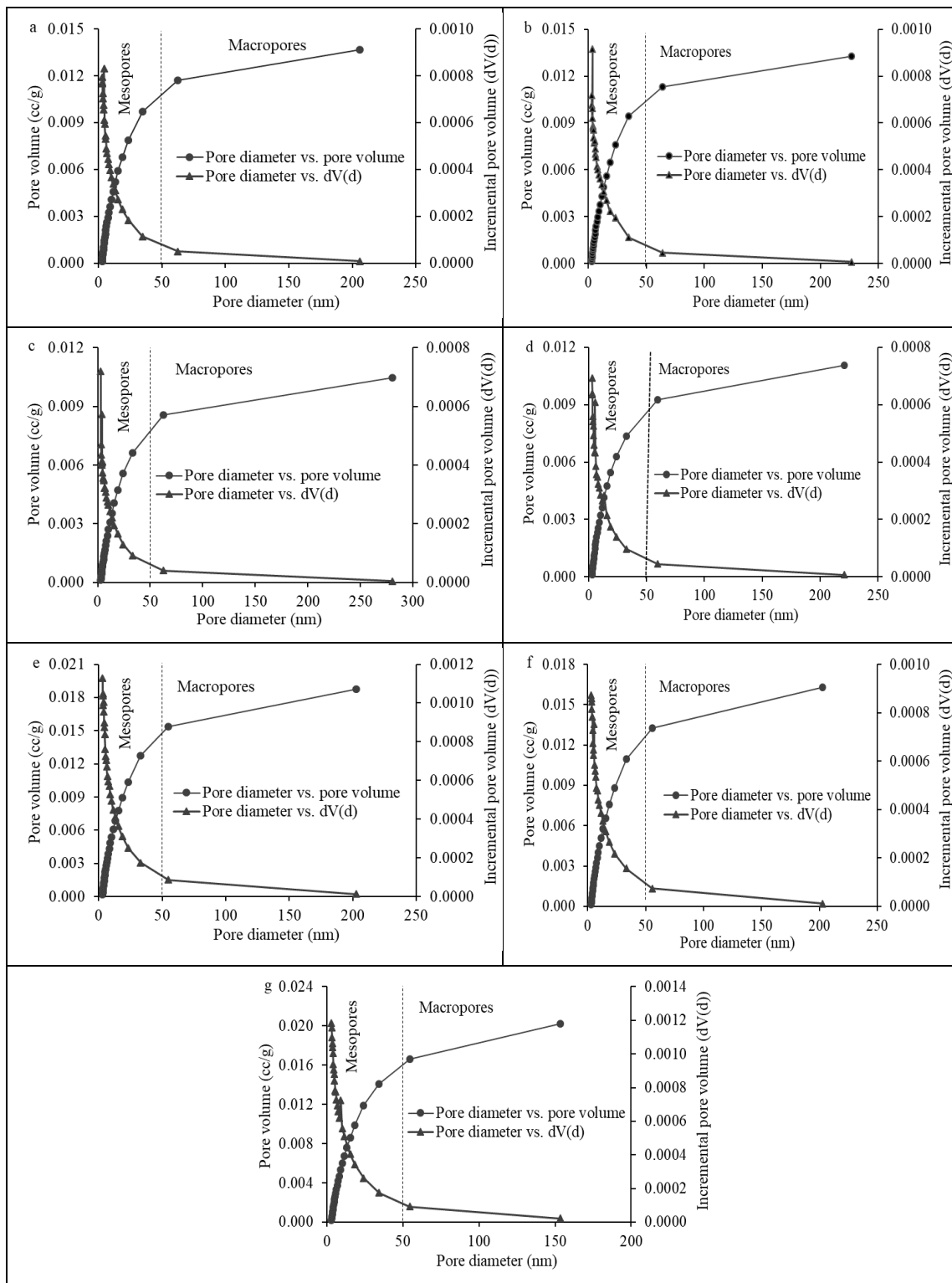


Fig. 7: BJH plots for pore size distributions for Barakar shales from Rajmahal Basin.

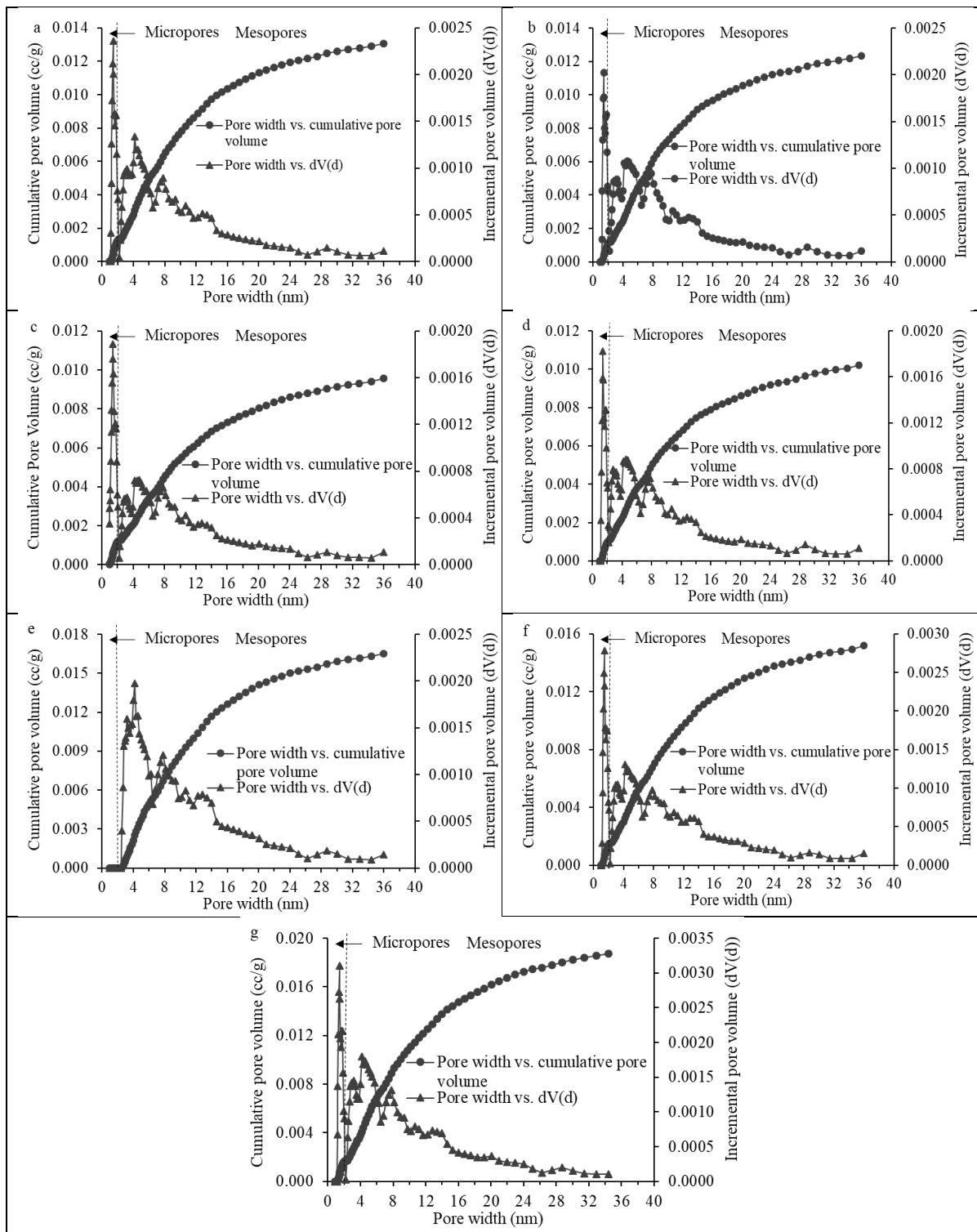


Fig. 8: DFT plots for pore volume distribution of Barakar shales from Rajmahal Basin.

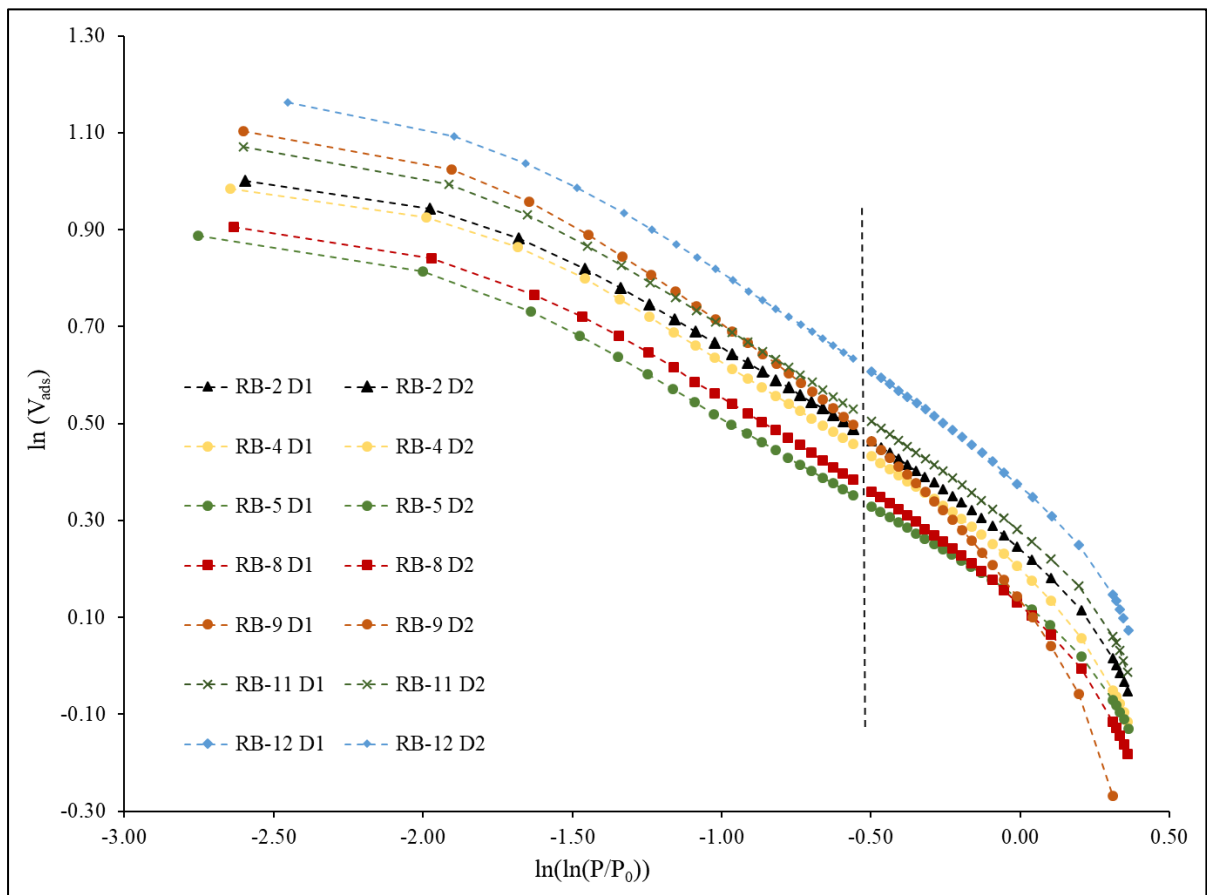


Fig. 9: The plots of $\ln(\ln(P_0/P))$ and $\ln(V_{ads})$ showing two distinct segments of fractal dimensions for Barakar shales.

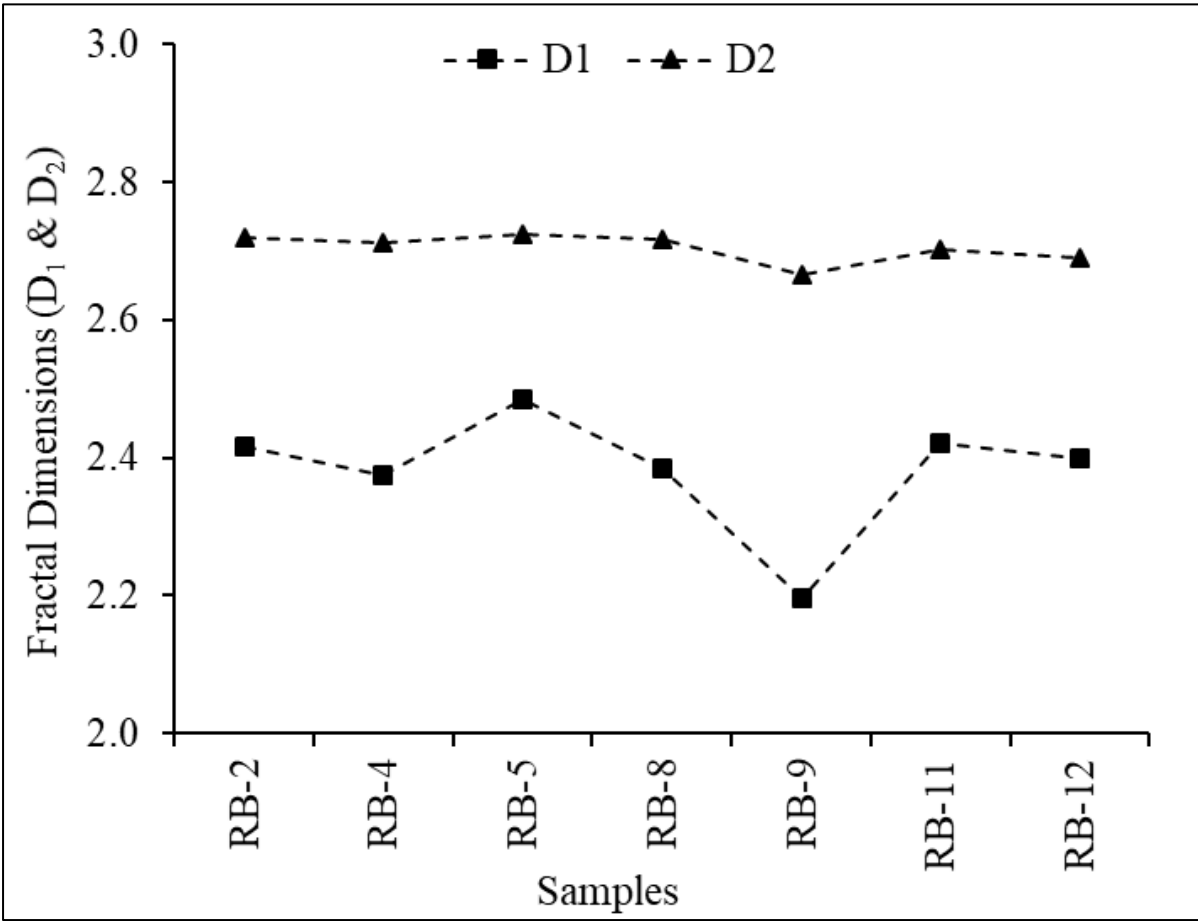


Fig. 10: Variation trend of fractal dimensions with samples.

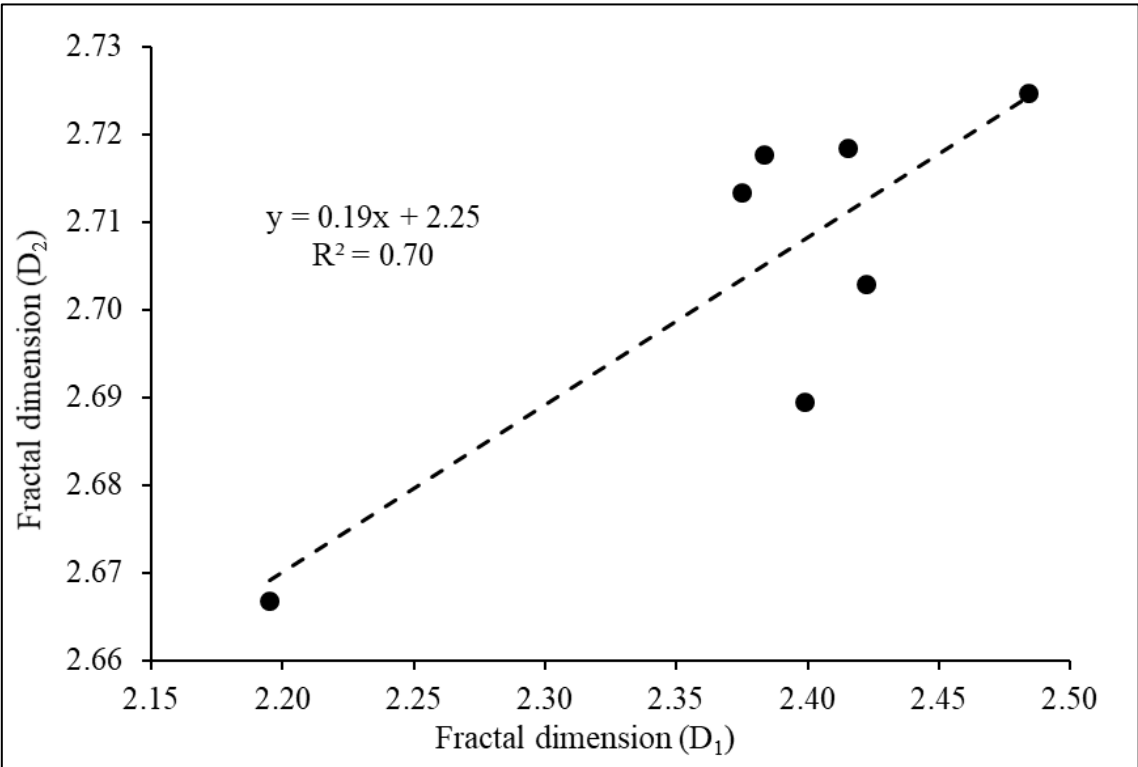


Fig. 11: The scatter plot showing the relation between fractal dimensions D_1 and D_2 .

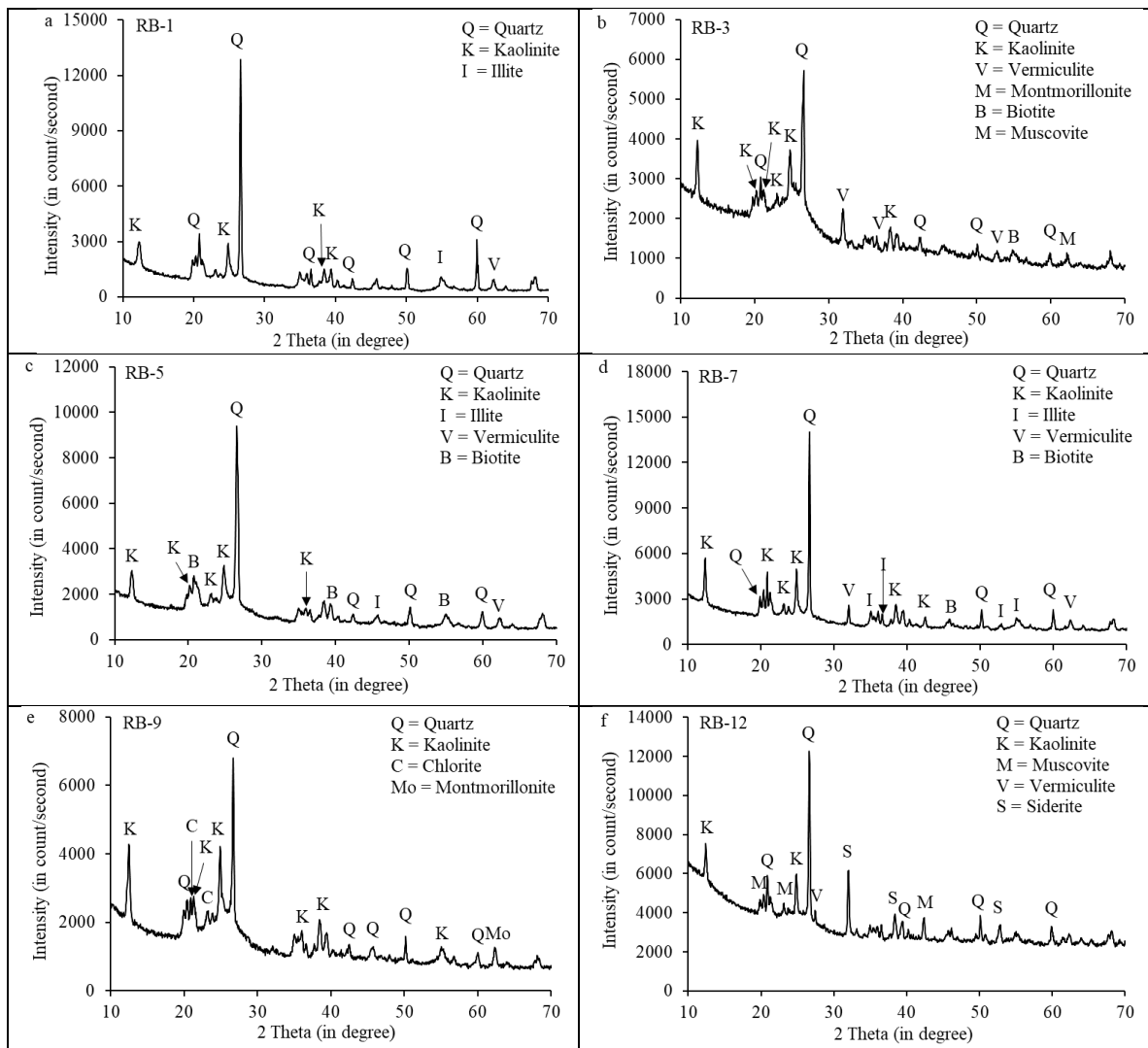


Fig. 12: XRD peaks showing the presence of clays and different mineral phases in Barakar shales.

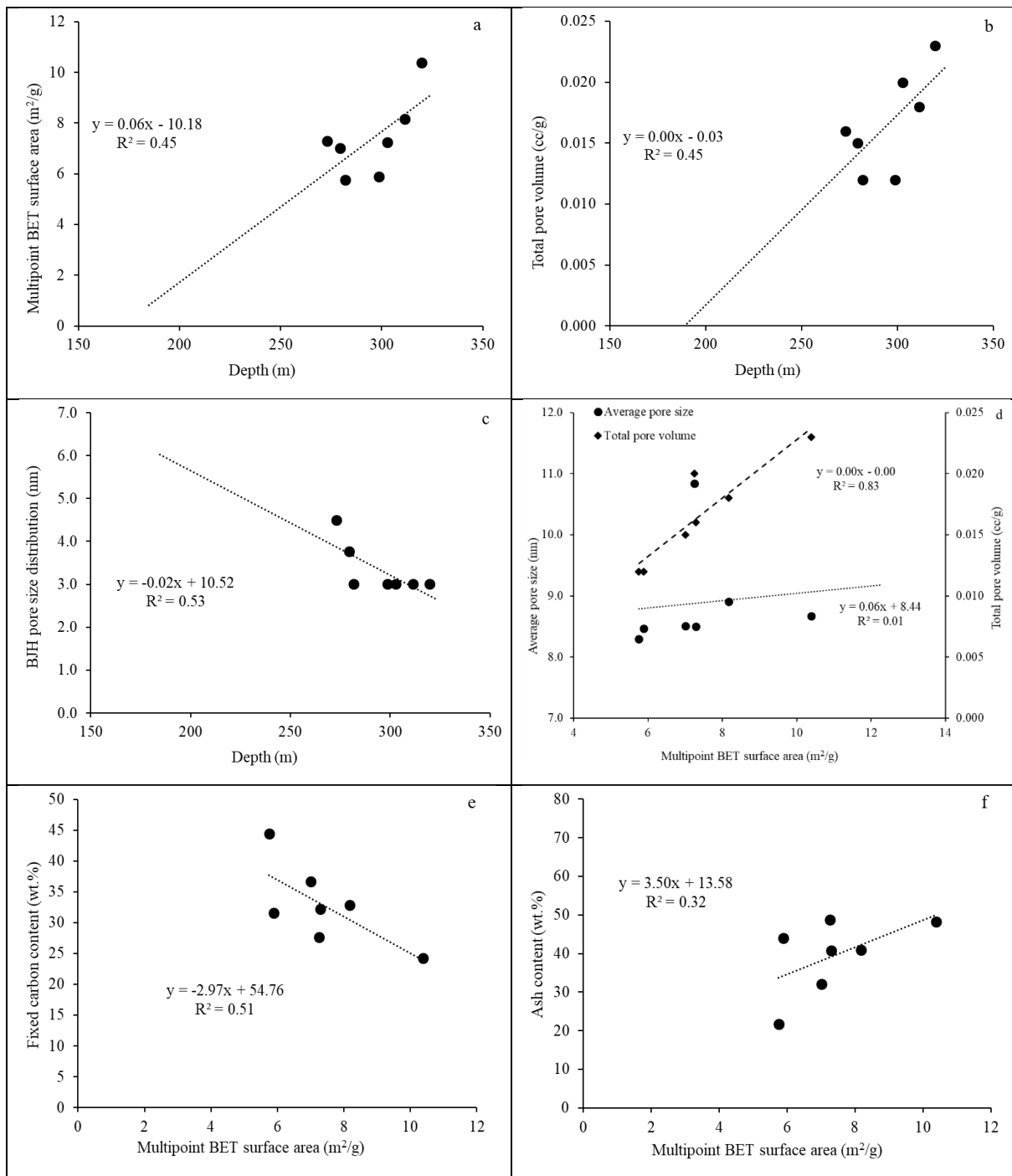


Fig. 13: Cross-plot showing the relation between the a) depth vs. multipoint BET surface area; b) depth vs.; total pore volume c) depth vs. BJH pore size; d) multipoint BET surface area vs. average pore size and total pore volume; e) multipoint BET surface area vs. fixed carbon content; f) multipoint BET surface area vs. ash content.

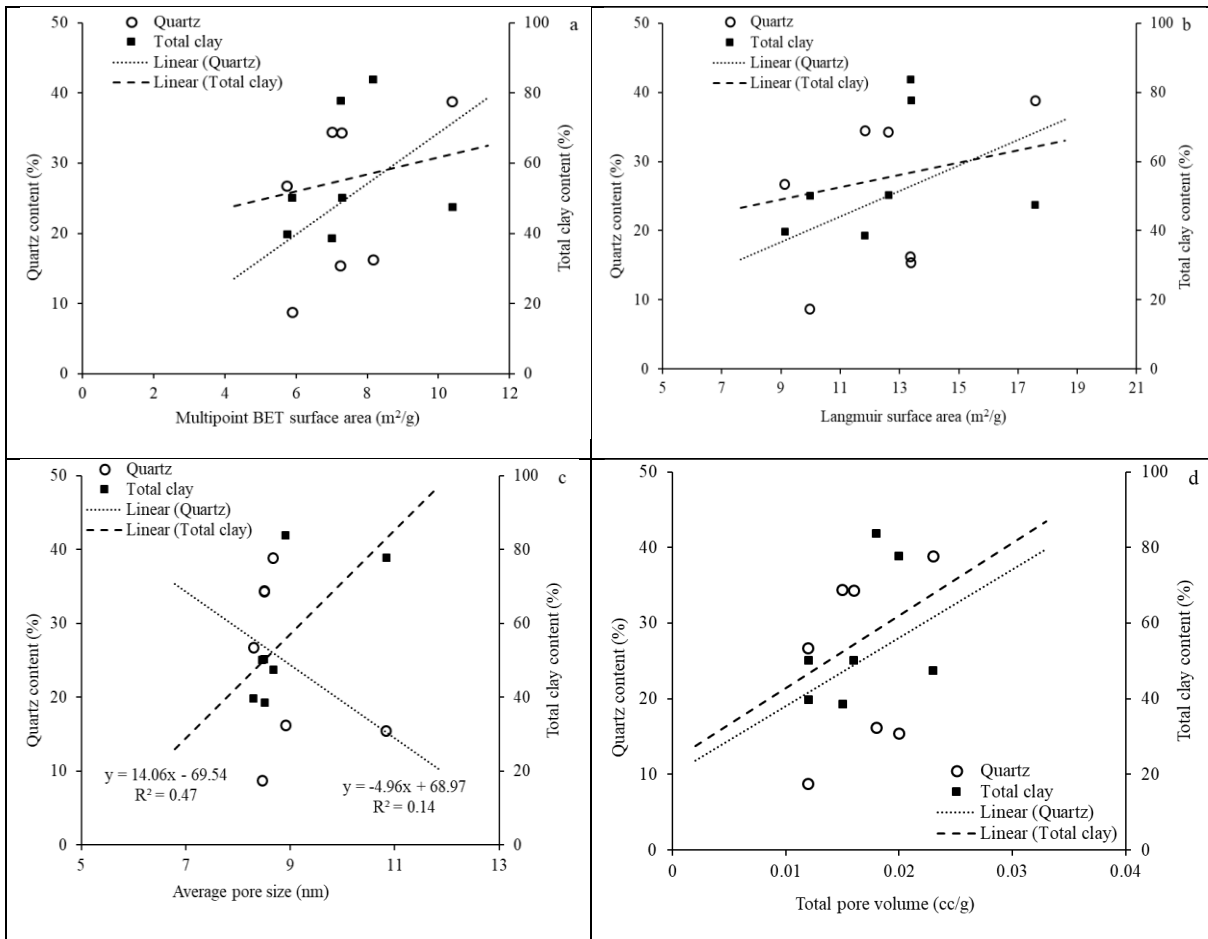


Fig. 14: Cross-plot showing the relation between the quartz and total clay with a) multipoint BET surface area; b) langmuir surface area; c) average pore size and d) total pore volume.

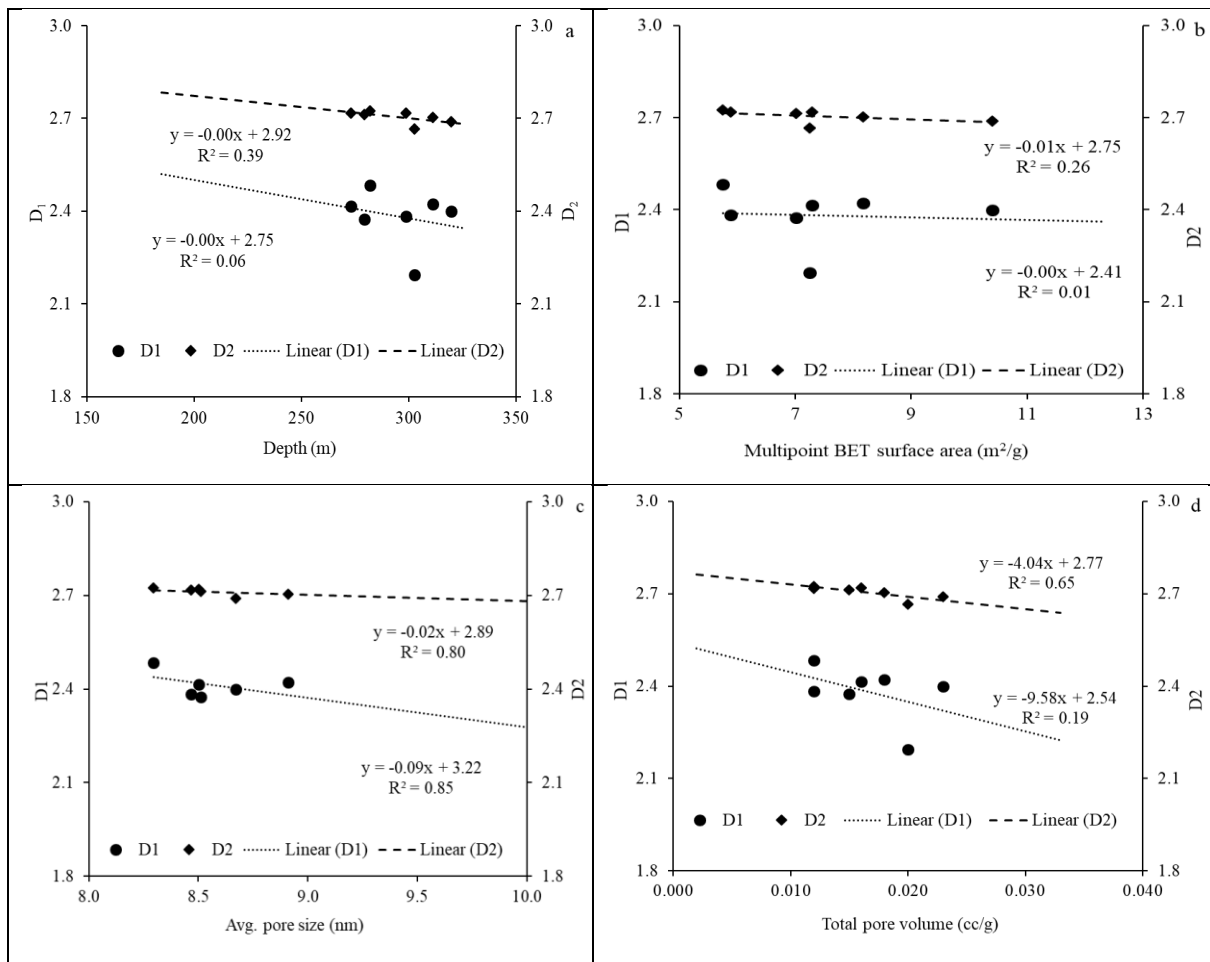


Fig. 15: Cross-plot showing the relation between the D_1 & D_2 with a) depth; b) multipoint BET surface area; c) average pore size; and d) total pore volume.